Shock Waves (2013) 23:619–634
DOI 10.1007/s00193-013-0472-5

ORIGINAL ARTICLE

Formation of particle jetting in a cylindrical shock tube

T. Xu · F.-S. Lien · H. Ji · F. Zhang

Received: 23 July 2012 / Revised: 11 July 2013 / Accepted: 17 August 2013 / Published online: 1 September 2013

Abstract A dense, solid particle flow is numerically studied at a mesoscale level for a cylindrical shock tube problem. The shock tube consists of a central high pressure gas driver section and an annular solid powder bed with air in void regions as a driven section with its far end adjacent to ambient air. Simulations are conducted to explore the fundamental phenomena, causing clustering of particles and formation of coherent particle jet structures in such a dense solid flow. The influence of a range of parameters is investigated, including driver pressure, particle morphology, particle distribution and powder bed configuration. The results indicate that the physical mechanism responsible for this phenomenon is twofold: the driver gas jet flow induced by the shock wave as it passes through the initial gaps between the particles in the innermost layer of the powder bed, and the chaining of solid particles by inelastic collision. The particle jet forming time is determined as the time when the motion of the outermost particle layer of the powder bed is first detected. The maximum number of particle jets is bounded by the total number of particles in the innermost layer of the powder bed. The number of particle jets is mainly a function of the number of particles in the innermost layer and the mass ratio of the powder bed to the gas in the driver section, or the ratio of powder bed mass (in dimensionless form) to the pressure ratio between the driver and driven sections.

Keywords Particle clustering · Particle jetting · Inelastic collision

Communicated by M. Brouillette.

T. Xu · H. Ji
Waterloo CFD Engineering Consulting Inc., 534 Paradise Cres., Waterloo, ON N2T 2N7, Canada
e-mail: taoxu@watcfd.com

H. Ji
e-mail: huaji@watcfd.com

F.-S. Lien (✉)
Department of Mechanical and Mechatronics Engineering, University of Waterloo, 200 University Avenue West, Waterloo, ON N2L 3G1, Canada
e-mail: fue-sang.lien@uwaterloo.ca; fslien@uwaterloo.ca

F. Zhang
DRDC-Suffield, PO Box 4000, Stn. Main, Medicine Hat, AB T1A 8K6, Canada
e-mail: Fan.Zhang@drdc-rddc.gc.ca

1 Introduction

It is widely observed in volcanic eruptions, supernovae and heterogeneous explosive detonations that the expansion of condensed-phase particles forms clusters and coherent jets. A coherent jet due to heterogeneous explosive detonation as shown in Fig. 1 consists of many clusters of particles. In the case of detonation of an explosive mixture containing densely-packed solid particles, particle clustering and jetting are generated at the very early stage of the particle dispersal process, which then persist for a long time (see, e.g., Fig. 1) [1–4]. The fundamental physics of this phenomenon puzzles many researchers, who have studied dense solid particle flows to-date. As a result, considerable efforts and research interests have been incurred in both experimental studies and numerical simulations to understand jetting formation mechanisms. Based on the experiments of spherical mitigated charges that consist of a central explosive surrounded by mitigants, Milne et al. [1] postulated that the jet structures must have already formed before the outer surface of the powder bed became unstable. Since the interface between the explosive charge and mitigants was invisible from their radiographs, the exact timing of the "early" time cannot be

Fig. 1 Explosive dispersal of a 2L cylindrical charge that consists of a small cylindrical C4 explosive packed in a central glass tube surrounded by an annulus of atomized dry aluminum particles [4]

determined experimentally. They also investigated the time scale associated with the instability, which contributed to the formation of jets, and speculated that the Rayleigh Taylor instability was not likely the cause of the formation of jet structures. Frost et al. [3] carried out a series of exploratory experiments of both spherical and conical charge configurations to gain insights into what caused the jet formation in densely-packed particle dispersion. They observed that the diameter and material density of the particle in a packed powder bed and the explosive mass significantly influenced the development of instabilities at the outermost surface of the expanding powder bed. They postulated that the number of jets formed was governed by a subtle balance between the detonation expansion (which tended to fracture layers of particles) and the viscous resistance of the shock-compacted powder bed. The ratio of particle expanding inertial force to viscous force during the shock compaction of the particle layers was represented by a particle compaction Reynolds number. When the compaction Reynolds number was below a certain threshold, the outer surface of the powder bed expanded smoothly and no jet structures were observed in the experiments. Zhang et al. [4] conducted a number of particle dispersal experiments using a cylindrical explosive surrounded by either a pure liquid, dry solid particles as exemplified in Fig. 1 or a mixture of both. A careful analysis of these trial data indicated that the powder bed fragmentation or the incipient number of particle jets was mainly dominated by the initial expansion velocity of the powder bed [5]. The experimental initial particle expansion velocity was found to be in good agreement with the so-called "Gurney velocity", which was determined by the mass ratio of the powder bed to the explosive. After the jet formation stage, the number of particle jets decreased with the dispersal distance from the center of the charge due to the late clustering and merging of particles as observed in the experiments, likely affected by the aerodynamic forces acting on particles. Ripley et al. [5] further performed two-phase CFD simulations incorporating a simple particle attraction model, which was designed to be proportional to the gradient of particle volume fraction and applied only in the jet formation phase. Their macroscopic numerical modeling results demonstrated that either the initial perturbations at the material interface or the simple particle attraction model could lead to clustering of particles and, hence, formation of coherent jets.

Despite the progress made to date in dense solid particle multiphase flow simulations, the true mechanisms causing particle jetting are still unknown due to the complex phenomena involved in the early phase of detonation expansion, including shock-particle interaction, particle collision and turbulence. Experimental visualization or diagnostics for the particle-jetting formation process at mesoscale are still very challenging. The mesoscale CFD simulations (albeit the total number of particles in the simulations is limited by the computer resources available), on the other hand, may be applied to track and visualize the particle trajectories caused by shock-particle and particle-particle interactions, thus helping elucidate the mechanisms that lead to clustering of particles and formation of particle jets. This tool can also be used to assist the development of improved drag-force and heat transfer models required in macroscopic multiphase-flow CFD codes, in which particle clustering and jetting are merely modeled through the momentum and energy exchange source terms in their respective momentum and energy equations.

In the present paper, a cylindrical shock tube using a packed annular particle bed (also referred to as a "powder bed" herein) placed in the driven section with its far end adjacent to ambient air is investigated. Note that any solid particle in the present shock tube problem is analogous to a large cluster of particles formed in an expanding powder bed in heterogeneous explosive detonation (see, e.g., Fig. 1). Numerical studies at mesoscale are performed over a range of parameters, including driver gas, particle morphology, particle distribution, and powder bed configuration, in order to understand the fundamental phenomena and physical mechanisms responsible for the clustering of particles and the formation of particle jet structure in the dense, solid particle flow as a result of shock compaction and expansion. The HLLC3D-IBM code is used, which is based on the monotone integrated large eddy simulation (MILES) approach [6] combined with the ghost-cell immersed boundary method (GCIBM) [7]. A novel multiple-particle collision model is proposed here to resolve explicitly shock-particle, particle-wake/boundary-layer and turbulence-particle interactions and inelastic particle collision. This code has been employed to conduct a

preliminary investigation of the physical mechanisms causing particle collision in post-detonation flows [8].

The paper is organized as follows: In Sect. 2, the numerical algorithms employed in the HLLC3D-IBM code for mesoscale simulations are described. In Sect. 3, the simulation results for a reference case, referred to as the "Basic" case, are then presented and the mechanisms responsible for the formation of particle jets are discussed. Extensive parametric studies to pinpoint the underlying physics, which controls the number of particle jets are addressed in Sect. 4. Finally, concluding remarks are drawn in Sect. 5.

2 Numerical approaches for mesoscale simulations

A two-dimensional cylindrical shock tube with a high-pressure driver section and a packed annular particle bed placed in the driven section with its far end adjacent to ambient air is investigated. The HLLC3D-IBM code is employed for the present study to model particle collision and agglomeration processes. The two-dimensional governing equations, satisfying mass, momentum and energy conservation laws, are given below,

$$\frac{\partial \mathbf{U}}{\partial t}+\frac{\partial \mathbf{E}}{\partial x}+\frac{\partial \mathbf{F}}{\partial y}=0 \tag{1}$$

where $\mathbf{U}$ is the vector of conservative variables (ρ, ρu, ρv, ρE), and $\mathbf{E}$ and $\mathbf{F}$ are given below

$$\mathbf{E}=\begin{pmatrix}\rho u\\ \rho u^2+p-\tau_{xx}\\ \rho uv-\tau_{xy}\\ (\rho E+p)u+\psi_x\end{pmatrix}\quad \mathbf{F}=\begin{pmatrix}\rho v\\ \rho uv-\tau_{xy}\\ \rho v^2+p-\tau_{yy}\\ (\rho E+p)v+\psi_y\end{pmatrix} \tag{2}$$

with

$$\begin{aligned}\psi_x &= -u\tau_{xx}-v\tau_{xy}+q_x\\ \psi_y &= -u\tau_{xy}-v\tau_{yy}+q_y\end{aligned} \tag{3}$$

The viscous stress tensor τ_{ij}, heat flux q_i and the equation of state (EOS) are written as:

$$\begin{aligned}\tau_{ij} &= \mu\left[\frac{\partial u_i}{\partial x_j}+\frac{\partial u_j}{\partial x_i}-\frac{2}{3}\left(\frac{\partial u_k}{\partial x_k}\right)\delta_{ij}\right]\\ q_i &= -k\frac{\partial T}{\partial x_i}\\ p &= (\gamma-1)\rho\left[E-\frac{1}{2}\left(u^2+v^2\right)\right]\end{aligned} \tag{4}$$

where μ is the dynamic viscosity, k is the thermal conductivity and γ is the specific-heat ratio. The HLLC approximate Riemann solver [9], combined with the MUSCL-Hancock method and an explicit time-stepping scheme, is used to achieve second-order accuracy of solutions in both space and time (details can be found in [10]).

A mesh containing highly-stretched cells adjacent to walls is usually required for a "wall-resolved" large eddy simulation (LES), which is computationally expensive and impractical to be considered for the present work involving many randomly moving particles on a (background) uniform Cartesian grid. Instead, the following simple log-law-based wall model (see, e.g., Sagaut [11]) is employed here:

$$U_t^+=\frac{U_t}{U_\tau}=\frac{1}{\kappa}\ln(Ey^+) \tag{5}$$

where U_t is tangential velocity, U_τ is the friction velocity, $E(\approx 9.8)$ is an empirical constant, $\kappa\approx 4.2$ is the von Karman constant, and y^+ is defined as

$$y^+=\frac{\rho U_t y}{\mu} \tag{6}$$

where y is the distance normal to the surface of a cylindrical particle. Based on the above assumptions, the above wall model can be implemented as follows:

1. Make an initial guess for U_τ.
2. Calculate y^+ using (6).
3. Calculate λ:

$$\begin{aligned}\lambda &= \frac{\mu}{y}, \quad \text{if } y^+\le 11.6\\ \lambda &= \frac{\rho U_\tau \kappa}{\ln\left(Ey^+\right)}, \quad \text{if } y^+>11.6\end{aligned} \tag{7}$$

4. Calculate $U_\tau=\sqrt{\frac{\lambda U_t}{\rho}}$.
5. Compare U_τ with its value in the previous iteration. If the difference is greater than the convergence threshold, go to step (3).
6. Calculate the additional source terms in the x- and y-momentum equations:

$$\begin{aligned}S_x &= -\mathrm{AREA}_x\rho U_\tau^2 u_t/|U_t|\\ S_y &= -\mathrm{AREA}_y\rho U_\tau^2 v_t/|U_t|\end{aligned} \tag{8}$$

where u_t, v_t are the x- and y-components of the tangential velocity vector $\mathbf{U}_t$, and AREA_x and AREA_y are the x- and y-projected areas on a solid boundary.

Equations (1)–(6) allow a high-resolution total variation diminishing (TVD)-based Navier–Stokes code to be used as the main numerical tool for the present simulations based on the concept of the MILES [12] in order to increase the overall computational efficiency. Here, we assume that the numerical viscosity associated with the 2nd-order TVD scheme based on the "minmod" limiter behaves like the sub-grid-scale (SGS) viscosity, and is sufficient to drain the turbulence energy in high-wave-number regimes.

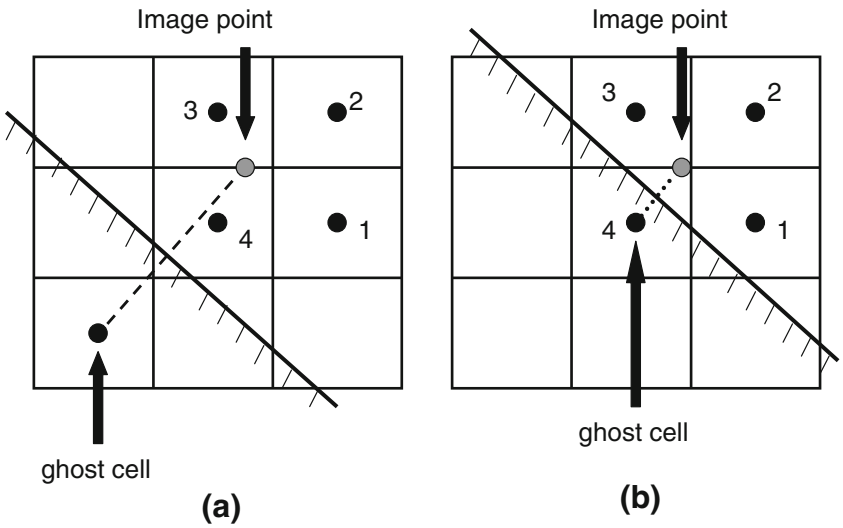

Fig. 2 Two sample cases in IBM to deal with an image point adjacent to a slanted wall: **a** four fluid cells surrounding the image point; **b** one of the cells surrounding the image point is a ghost cell

To effectively simulate moving circular particles on a (background) Cartesian mesh, the GCIBM proposed by Tseng and Ferziger is implemented in the code [7]. The key idea of GCIBM is to calculate the numerical boundary conditions in the ghost cells, and it involves two major steps. The first step is to use the "ray-tracing" technique to flag the ghost cells, and the second step is to determine the image (or mirror) point in the fluid region corresponding to the centroid of each ghost cell lying in the solid region. The numerical value of the solution variable at each image point is evaluated by using a bilinear interpolation based on the four surrounding nodal values. Specific implementation details for a two-dimensional inviscid flow are described below by reference Fig. 2a for illustration purposes:

1. The velocity vector at solid boundaries, $\mathbf{U}_\mathrm{B} = u^t_\mathrm{B}\mathbf{e}^t + u^n_\mathrm{B}\mathbf{e}^n$ (where $\mathbf{e}^t$ and $\mathbf{e}^n$ are the unit vectors tangential and normal to walls, respectively) is split into its tangential and normal components $(u^t_\mathrm{B}, u^n_\mathrm{B})$ satisfying the "slip condition" and the "impermeability condition":

$$\frac{\partial u^t_B}{\partial n} = 0 \simeq \frac{u^t_I - u^t_G}{\Delta n}, u^n_B = 0 \simeq \frac{1}{2}\left(u^n_G + u^n_I\right) \tag{9}$$

The subscripts "G" and "I" in (9) denote the value at the "ghost" and "image" locations, respectively, and Δn is the normal distance between the ghost and image nodes. Equation (9) above can be re-written as follows to determine the boundary conditions at ghost cells:

$$u^t_G = u^t_I, u^n_G = -u^n_I \tag{10}$$

where $u^t = un^y - vn^x$, $u^n = un^x + vn^y$, and $\mathbf{n} = n^x\mathbf{e}^x + n^y\mathbf{e}^y$ is the unit vector normal to walls. $\mathbf{e}^x$ and $\mathbf{e}^y$ are the unit vectors in the x- and y-directions, respectively. Note that the velocity vector $\mathbf{U} = u^t\mathbf{e}^t + u^n\mathbf{e}^n = u\mathbf{e}^x + v\mathbf{e}^y$.

2. The values of u^t and u^n at the image point are determined by using the following bilinear interpolation formula:

$$\phi(x, y) = C_1 + C_2x + C_3y + C_4xy \tag{11}$$

in which $\phi = u^t$ or u^n. The coefficients C_1–C_4 can be obtained from

$$\begin{bmatrix} C_1 \\ C_2 \\ C_3 \\ C_4 \end{bmatrix} = \begin{bmatrix} 1 & x_1 & y_1 & x_1 & y_1 \\ 1 & x_2 & y_2 & x_2 & y_2 \\ 1 & x_3 & y_3 & x_3 & y_3 \\ 1 & x_4 & y_4 & x_4 & y_4 \end{bmatrix}^{-1} \begin{bmatrix} \phi_1 \\ \phi_2 \\ \phi_3 \\ \phi_4 \end{bmatrix} \tag{12}$$

where $\phi_1, \phi_2, \phi_3, \phi_4$ are ϕ at the centroid of four cells surrounding the image point, and then ϕ at the image location can be calculated by

$$\phi_I = C_1 + C_2x_I + C_3y_I + C_4x_Iy_I \tag{13}$$

3. The Cartesian velocity components (u, v) at the ghost point, used as the boundary conditions for the momentum equations, are

$$u_G = u^t_I n^y - u^n_I n^x, v_G = -\left(u^t_I n^x + u^n_I n^y\right) \tag{14}$$

However, if one of the four cells surrounding the image point is a ghost cell, a special treatment is needed as explained below by reference to Fig. 2b. As seen, $\phi_4 \equiv \phi_G$ is a ghost cell. If $\phi_G = u^t_G = u^t_I$ (satisfying the slip condition) from (11), we can derive

$$\begin{bmatrix} C_1 \\ C_2 \\ C_3 \\ C_4 \end{bmatrix} = \begin{bmatrix} 1 & x_1 & y_1 & x_1 y_1 \\ 1 & x_2 & y_2 & x_2 y_2 \\ 1 & x_3 & y_3 & x_3 y_3 \\ 0 & x_G - x_I & y_G - y_I & x_G y_G - x_I y_I \end{bmatrix}^{-1} \begin{bmatrix} \phi_1 \\ \phi_2 \\ \phi_3 \\ 0 \end{bmatrix} \tag{15}$$

Similarly, if $\phi_G = u_G^n = -u_I^n$ (satisfying the impermeability condition), then

$$\begin{bmatrix} C_1 \\ C_2 \\ C_3 \\ C_4 \end{bmatrix} = \begin{bmatrix} 1 & x_1 & y_1 & x_1 y_1 \\ 1 & x_2 & y_2 & x_2 y_2 \\ 1 & x_3 & y_3 & x_3 y_3 \\ 2 & x_G + x_I & y_G + y_I & x_G y_G + x_I y_I \end{bmatrix}^{-1} \begin{bmatrix} \phi_1 \\ \phi_2 \\ \phi_3 \\ 0 \end{bmatrix} \tag{16}$$

Once we have determined u_I^t and u_I^n by (13), (15) and (16), we can calculate u_G and v_G from (14). If two or more cells surrounding the image point are ghost cells, similar special treatments can also be derived.

The test case of shock diffraction over a circular cylinder at Mach number 2.81 was performed on four different grids of 200 × 200, 250 × 250, 300 × 300 and 400 × 400 nodes, respectively. Only results for the last two fine grids are shown in Fig. 3. As seen, a triple point occurs where the incident, Mach shock and reflected shock intersect. The triple-point path is tangent to the cylinder at an angle of 30.6° on a mesh of 300 × 300 nodes and 30.7° on a mesh of 400 × 400 nodes, an observation/result which agrees fairly well with the result of 30.8° reported by Ripley et al. [12] obtained with an unstructured-grid method.

A multi-particle collision model is crucial in the investigation of mechanisms for clustering and agglomeration of particles and formation of particle jets in a dense solid particle flow. The traditional collision model described in (17) below is only valid for a two-particle collision. When two particles collide with each other, particle velocities at pre- and post-collision instants can be determined by the following model, which assumes that the two hard, spherical particles can instantaneously change their velocities upon collision [13]:

$$\begin{aligned} \mathbf{u}'_{\mathrm{p},1} &= \mathbf{u}_{\mathrm{p},1} - \frac{m^{\mathrm{eff}}}{m_{\mathrm{p},1}}(1+\varepsilon)(\mathbf{u}_{\mathrm{p},12}\cdot\mathbf{e})\mathbf{e} \\ \mathbf{u}'_{\mathrm{p},2} &= \mathbf{u}_{\mathrm{p},2} + \frac{m^{\mathrm{eff}}}{m_{\mathrm{p},2}}(1+\varepsilon)(\mathbf{u}_{\mathrm{p},12}\cdot\mathbf{e})\mathbf{e}, \end{aligned} \tag{17}$$

where the effective mass is

$$m^{\mathrm{eff}} = \frac{m_{\mathrm{p},1} m_{\mathrm{p},2}}{m_{\mathrm{p},1} + m_{\mathrm{p},2}} \tag{18}$$

and ε is the restitution coefficient. The velocity vector with the superscript of prime stands for the post-collision velocity vector. Note that for $\varepsilon = 1$, the total kinetic energy is conserved, and the collision occurs elastically. $e = \frac{\mathbf{r}_1 - \mathbf{r}_2}{|\mathbf{r}_1 - \mathbf{r}_2|} = \frac{\mathbf{r}_{12}}{|\mathbf{r}_{12}|}$, where $\mathbf{r}_{12}$ is the vector which joins the centers of particles at the very moment when they come into contact. $\mathbf{u}_{\mathrm{p},12} = \mathbf{u}_{\mathrm{p},1} - \mathbf{u}_{\mathrm{p},2}$ is the relative velocity of two particles before collision. For two particles with the same size, the post-elastic collision velocity can be derived from (17) and (18) as,

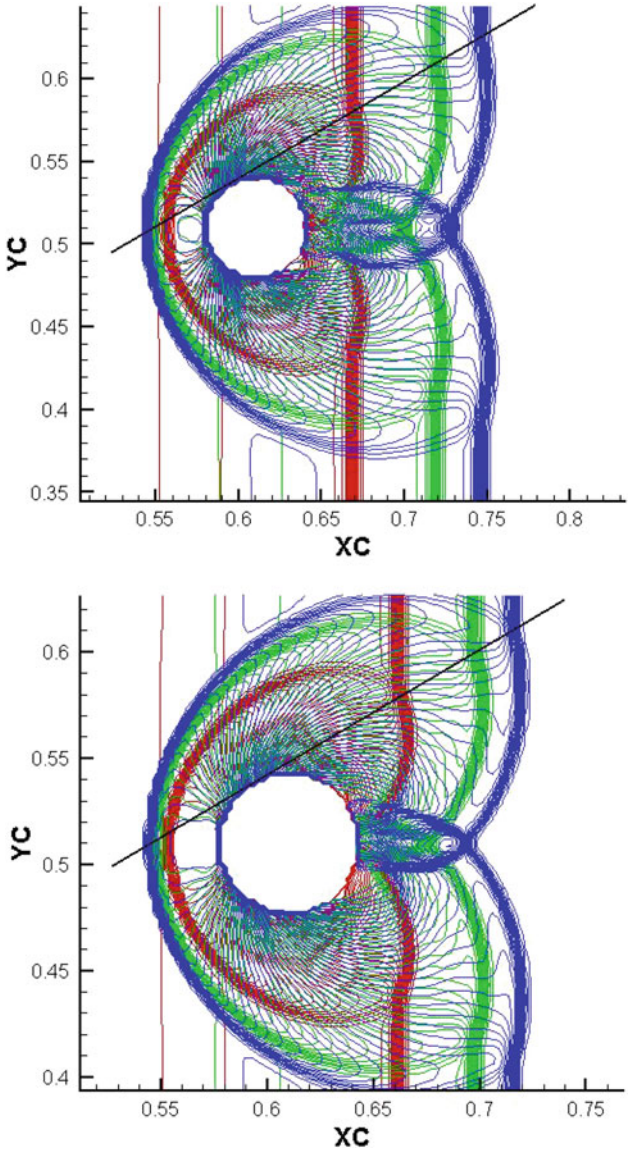

Fig. 3 Shock diffraction over a circular cylinder at Mach 2.81 on two different grids: 300 × 300 nodes (*top*) and 400 × 400 nodes (*bottom*). XC and YC are nondimensionalized based on the cylinder diameter

$$\begin{aligned} \mathbf{u}'_{\mathrm{p},1} &= \mathbf{u}_{\mathrm{p},2} \\ \mathbf{u}'_{\mathrm{p},2} &= \mathbf{u}_{\mathrm{p},1} \end{aligned} \tag{19}$$

If $\varepsilon = 0$, the complete energy associated with the relative motion is lost or dissipated, and the particles are bound together after a collision, which is classified as an inelastic collision. For two particles with the same size, the

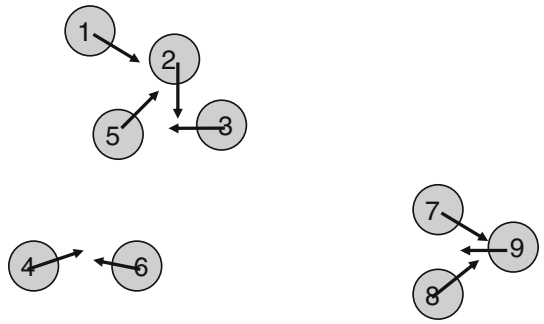

Fig. 4 Illustration of collision of multiple particles at a given time step

Table 1 A list of two-particle collision scenarios shown in Fig. 4

Collision no.	Particle no.	Particle no.
Collision #1	1	2
Collision #2	2	3
Collision #3	2	5
Collision #4	7	8
Collision #5	8	9
Collision #6	4	6

post-inelastic collision velocity can be derived from (17) and (18) as,

$$\mathbf{u}'_{\mathrm{p},1} = \mathbf{u}'_{\mathrm{p},2} = \frac{1}{2}\left(\mathbf{u}_{\mathrm{p},1} + \mathbf{u}_{\mathrm{p},2}\right) \tag{20}$$

Equations (17) and (18) are extended to handle multiple particle collisions in this work. If several particles collide inelastically at the same time, the post-collision velocity of all particles involved is the (weighted) average of the pre-collision particle velocities. A group of colliding particles sticking together will form as observed in the experiments. In the next time step, however, the group of (agglomerated) particles will possibly collide with other particles, which were not involved in the previous collision, or two or more groups of particles may collide and merge to form an even bigger group. This can introduce significant algorithmic complexity when implementing the GCIBM method. A recursive approach is therefore required to check each particle group until all particles in the post-collision phase satisfy the (numerical) collision criterion; namely, collision is considered occurring if the distance between centroids of two adjacent cylindrical particles is less than about $1.1d_{\mathrm{p}}$. The factor 1.1 here is somewhat arbitrary, depending on the number of grid cells used to explicitly resolve each particle in the computational domain.

Figure 4 exemplifies multiple particle collisions in a particle-laden flow. According to the above collision criterion, the number of two-particle collisions can be counted and listed in Table 1. The two-particle collision scenarios listed in Table 1 can be subdivided into three groups as illustrated in Table 2, in which the particle numbers (by reference to Fig. 4) involved in each group are given. Take group #1 involving 4 particles as an example. From Table 1, we notice that particle 2 is involved in two-particle collision scenarios #1 and #2. This implies that particles 1, 2 and 3 can form a group of three particles. Since particle 2 is also involved in two-particle collision scenario #3, we then increase the size of the aforementioned group by including particle 5 as well. This results in group #1 in Table 2, containing particles #1, #2, #3 and #5. Similar arguments apply to groups #2 and #3 in Table 2. Finally, the number of total particles involved in each group due to multiple particle collisions is counted and listed in Table 3, based on the results given in Table 2.

Table 2 A list of multi-particle collision groups shown in Fig. 4

Group no.	Particle no.	Particle no.	Particle no.	Particle no.
Group #1	1	2	3	5
Group #2	7	8	9	–
Group #3	4	6	–	–

Table 3 The number of particles for each collision group shown in Fig. 4

Group no.	Number of particles
Group #1	4
Group #2	3
Group #3	2

Let us assume all particles have the same mass, size and shape, and only inelastic collision ($\varepsilon = 0$) is considered here. In the case of two-particle collision, from (17) and (18), the post-collision particle velocity is equal to the arithmetic average of two pre-collision particle velocities. Similarly, according to the conservation of momentum, the post-collision particle velocity in multi-particle collision scenarios can be derived to be the arithmetic average of all pre-collision particle velocities involved:

$$u_{\mathrm{post}} = \frac{\sum_{i=1}^{n} u^i_{\mathrm{pre}}}{n}, \tag{21}$$

where u_{post} is the post-collision velocity for all particles and u^i_{pre} is the pre-collision velocity for particle i.

An upper limit for the time step is required in the simulations in order to keep the code numerically stable. This upper limit is given below:

$$\Delta t = \frac{\mathrm{CFL}\sqrt{\frac{(\Delta x)^2+(\Delta y)^2}{2}}}{\left(\sqrt{u^2+v^2}\right)_{\max}} \tag{22}$$

where Δx and Δy are the grid cell dimensions in the x- and y-directions, respectively, $\left(\sqrt{u^2+v^2}\right)_{\max}$ is the maximum post-collision velocity of particles, and CFL $\approx$0.5.

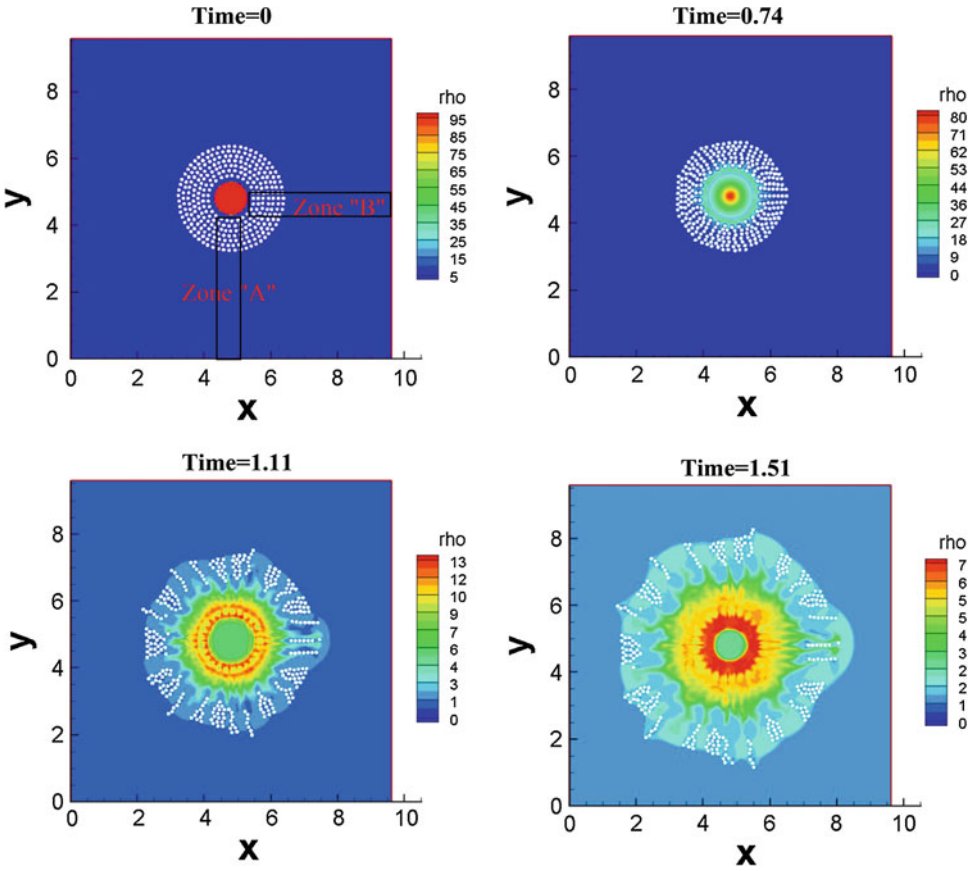

Fig. 5 Dimensionless density contours of particle dispersal at four different times for the "Basic" test case with 300 particles in the solution domain. Dimensionless groups are defined in (24). Time = 0 corresponds to the initial condition, where density and pressure ratio are defined in Table 5

To compute numerous scenarios efficiently for the present shocked dense particle flows, the HLLC3D-IBM code is parallelized and run on a shared-memory machine in SHARCNET (https://www.sharcnet.ca) using OpenMP.

3 Mechanisms for the formation of particle jet structure

The computational domain for the baseline test case (referred to as the "Basic" case in Table 5) of the present cylindrical shock tube problem is depicted in Fig. 5 (at $t = 0$ and at three other times). The domain includes a circular high pressure gas driver section and an annular driven section, the latter consisting of a solid powder bed filled with air in void regions adjacent to the driver section. In the far field of the driven section, the standard temperature and pressure (STP) condition for air is assumed: 1 atm and 25 °C. The air is assumed to follow the ideal gas law. This "Basic" test case contains 300 particles in 7 layers, and the corresponding particle volume fraction in the powder bed is 0.33. Table 4 lists the total number of particles in each ring-shaped layer and the radius of each layer from the center of the (cylindrical) driver section. The polar angle from the center of the particle to a horizontal datum line passing through the center of the driver section is defined by,

Table 4 The configuration of particle layers in a powder bed for the "Basic" test case

Layer no.	Number of particles	Radius
1	25	0.684
2	31	0.832
3	40	0.980
4	43	1.128
5	48	1.270
6	54	1.414
7	59	1.560

$$\theta_i = i\frac{2\pi}{N} \tag{23}$$

where i is the ith particle in the layer counted from the horizontal datum line in the counter-clockwise direction, and N is the total number of particles in that layer. Equation (23) ensures uniform angular distribution of particles in different layers, each with a different radius as indicated in Table 4. The size of the computational domain is 9.6×9.6 (in dimensionless units) covered with $1{,}000 \times 1{,}000$ structured grid cells for all test cases in this paper. The Neumann boundary conditions are applied to all far-field boundaries.

The typical grid resolution to cover a particle in the present study is about 25×25. Although LES should be three-dimensional and there is no doubt that "two-dimensional" (or 2-D) LES is fundamentally incorrect (key features, such

Table 5 The test matrix and conditions

Test case title	Total particles in domain	Gas pressure and density ratio	Particle radius	Restitution coefficient	Randomness	Particle density	Number of particle jets	Number of particle jets from (34)	Particle volume fraction
Basic	300	100:1	0.05	0	No	10	23	23	0.33
Layer3[a]	96	100:1	0.05	0	No	10	25	24	0.30
Layer5[b]	187	100:1	0.05	0	No	10	24	23	0.31
Particle density	300	100:1	0.05	0	No	10 and 50	22	23	0.33
Particle size	300	100:1	0.05 and 0.03	0	No	10	23	22	0.22
Pressure2	300	10:1	0.05	0	No	10	18	18	0.33
Pressure3	300	1000:1	0.05	0	No	10	25	24	0.33
Random	300	100:1	0.05	0	Yes	10	21	–	0.33
Restitution	300	100:1	0.05	0.5	No	10	23	–	0.33
Inner layer[c]	183	100:1	0.1	0	No	10	17	15	0.56

The radius of the driver section is 0.5 for all cases except the "Inner layer" case, where the corresponding radius is 0.8 to accommodate larger particles. All quantities in the table are dimensionless as defined in (24)

[a] The first 3 layers in Table 4 are included in the domain

[b] The first 5 layers in Table 4 are included in the domain

[c] 6 particle layers and 17 particles in the innermost layer of the powder bed, while all other cases in Table 5 have 25 particles in the innermost layer

as transition and vortex stretching cannot be captured by any 2-D LES), the reason why we still performed 2-D LES on a grid of 1,000 × 1,000 cells in the present study was mainly due to the limitation of computational resources available for numerous runs over a long period of time. It is noted that Bouris and Bergeles [14] reported in their 2-D LES for a turbulent flow over a square cylinder that the Strouhal number, drag coefficient, and mean velocity and total fluctuation energy (periodic plus turbulent) were fairly well predicted against the experimental data, which were much better in comparison with several RANS solutions. Therefore, we believe that the present 2-D LES based on the MILES approach can still be used to investigate qualitatively the mechanisms in relation to the formation of particle jets at mesoscale.

Note that the initial conditions and results presented in this paper are dimensionless. The dimensionless groups are defined as:

$$t^* = \frac{t a_r}{D_c};\ \rho^* = \frac{\rho}{\rho_r};\ u^* = \frac{u}{a_r};\ p^* = \frac{p}{\rho_r a_r^2};$$
$$F^* = \frac{F}{\rho_r a_r^2 D_c^2};\ M^* = \frac{M}{\rho_r D_c^3} \tag{24}$$

where t^*, ρ^*, u^* and p^* are the dimensionless time, density, velocity, pressure, force and mass, respectively. a_r is the reference speed of sound (346 m/s here), D_c is the diameter of the circular driver section and ρ_r is the reference density (i.e., the air density in the STP condition). The dimensionless symbol "$*$" is removed hereafter for simplicity. The parameters corresponding to the "Basic" test case are listed in the first row of Table 5.

Figure 5 shows the simulated particle dispersal process for the "Basic" test case at four different (dimensionless) times: $t = 0$, 0.74, 1.11 and 1.51. At the beginning, the high pressure driver gas is squeezed into the powder bed, and several micro gas jets between the solid particles are formed within the first layers. The resulting shock fronts are propagating radially in voids between particles (at $t = 0.74$). At the same time, the high pressure gas drives particles to form a chain of particles (see, e.g., $t = 1.11$ and 1.51) through collision. This results in the motion of particles in the outermost layer of the powder bed ahead of shocks. The shocked flow driven by the gas jets emanating from voids between particles, and the solid chaining of particles generated by collision fracture the powder bed, thus forming clusters of particles (or particle jets) as shown in Fig. 5 at $t = 1.11$. The total number of particle jets remains the same in the present case at a later time of $t = 1.51$. Note that the "staircase" structure observed in the contour plots of Fig. 5 (and Figs. 6, 7, 8, 9 later) is an artifact due to the plotting utilities used. This is because the solutions are obtained at centroids of the background *Cartesian* mesh when IBM is employed. There are no contours (viz., only the background white color is shown) inside particles. We use the "Blanking" function in tecplot (http://www.tecplot.com/) to skip the data inside the particles.

In order to better understand the physical mechanisms resulting in particle clustering and jetting, two rectangular (spatially-fixed) Eulerian zones are taken from the "Basic" test case as shown in Fig. 5 (at $t = 0$): zone A in the 6 o'clock (or south) direction and zone B in the 3 o'clock (or east) direction. The density contours of zones A and B from $t = 0$ to $t = 1.91$ are presented in Figs. 6 and 7, respectively. Note

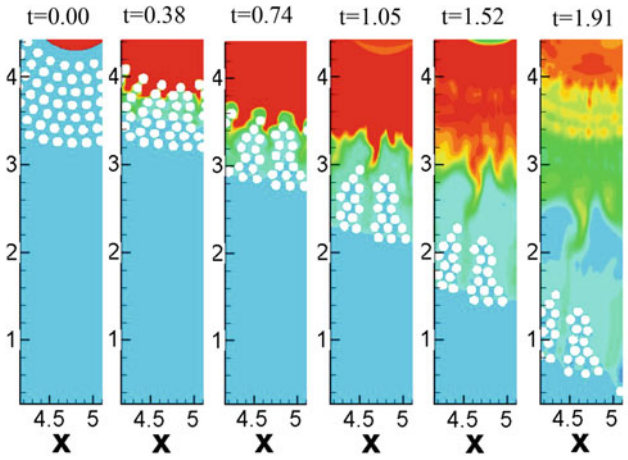

Fig. 6 The time evolution of dimensionless density contours in Zone A for the "Basic" test case. Dimensionless groups are defined in (24). Time = 0 corresponds to the initial condition, where density and pressure ratio are defined in Table 5

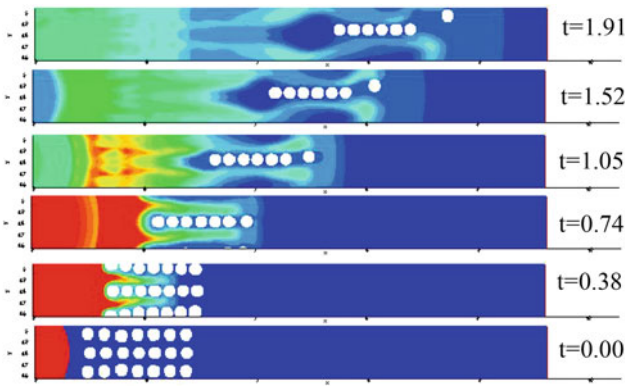

Fig. 7 The time evolution of dimensionless density contours in Zone B for the "Basic" test case. Dimensionless groups are defined in (24). Time = 0 corresponds to the initial condition, where density and pressure ratio are defined in Table 5

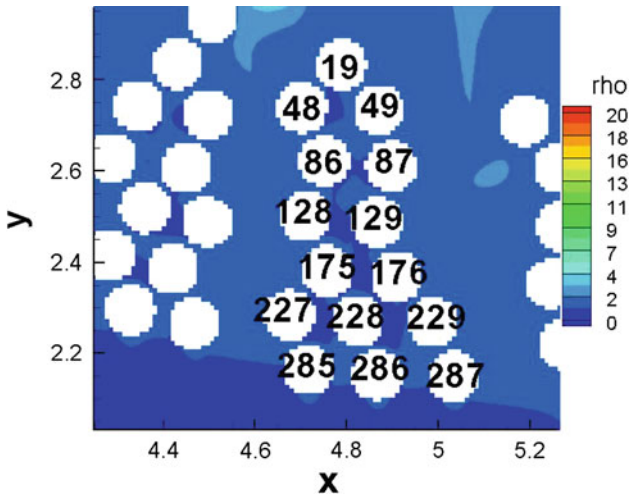

Fig. 9 Particles involved in a particle jet in Zone A are numbered for the "Basic" test case. Density (or "rho") is nondimensionalized using (24)

that Zones A and B were selected arbitrarily for illustration purposes, and the size of these zones was deliberately chosen so that at least one particle jet could be observed.

As shown in Fig. 6, the driver gas centered at the location of $(x, y) = (4.8, 4.8)$ in Zone A is released after $t = 0$. The interface between the driver section and the powder bed is disturbed due to the passage of the shock. The spike-like structures of gas at the interface emerge in void regions between particles in the innermost layer of the powder bed, and develop into incipient micro gas jets, which can be observed at $t = 0.38$. As the shock fronts propagate through the powder bed, the expanding gas jets and the flow ahead separate the particles, while the inelastic collision results in agglomeration of particles. The particle-to-particle interactions cause the outermost layer of the densely-packed powder bed to move ahead of the shock fronts as seen at $t = 0.74$. It is

Fig. 8 Initial perturbations of dimensionless density contours near the interface between the high-pressure and high-density driver section and particle layers. Dimensionless groups are defined in (24)

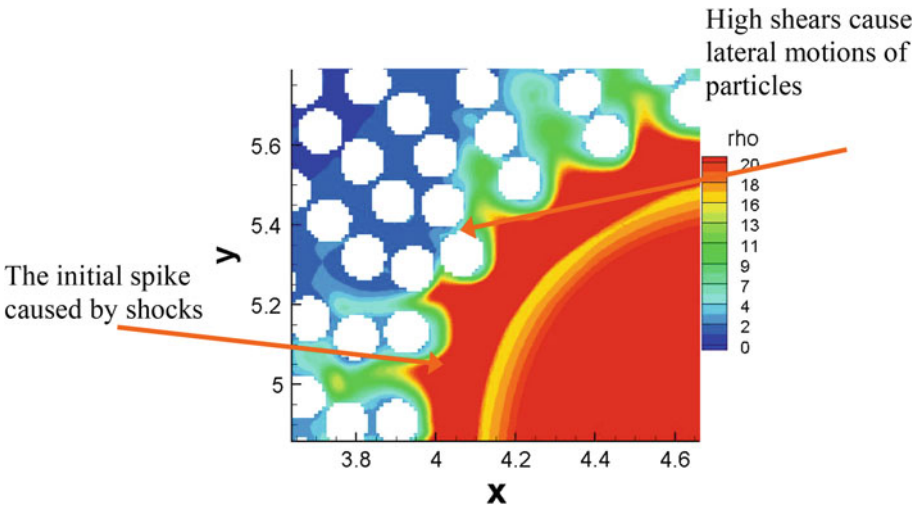

clear from the subfigure at $t = 0.74$ that the incipient particle jets have already formed. Based on this observation, the exact time corresponding to the formation of particle jet structure can be defined as the time when the outer surface of the powder bed is being perturbed. The spikes [i.e., the heavy (or high-density) fluid penetrating into the light (or low-density) fluid [15]] or bubbles (i.e., the light fluid penetrating into the heavy fluid [15]) disturbed by shocks lead to large shears between particles and their surrounding fluid, thus providing additional lateral forces acting on the particles. At $t = 1.05$, the voids between clusters of particles (or particle jets) due to inelastic collision can be clearly seen. The inter-particle forces at this time cancel each other within the agglomerated particles. At a time between 1.52 and 1.91, the jet structure is maintained and, each particle jet (typically containing 7–15 particles) moves outwards (or radially) in time.

The spike-like gas structures between the moving particles are initially induced by the passage of shocks, which develop later into the incipient micro gas jets. The micro-jet structure as observed in the innermost layer of the powder bed is triggered as the interface between heavy gas (in the driver section) and light gas (in the driven section) is impulsively accelerated. Most of the research about the Richtmyer–Meshkov (RM) instability was focused on single-phase flows, and analysis of multiphase RM instability is still in its infancy (see, e.g., [16,17]). The Rayleigh–Taylor (RT) instability between the high density gas in the driver section and its surrounding low density air is not likely the underlying mechanism for the formation of particle jets, because the time scale corresponding to the fracturing of the powder bed demonstrated here is much smaller than that for the growth of RT instability [1]. Furthermore, the present mesoscale results show that the maximum velocity of the gas jets is about 1.9, while the maximum velocity of particles in Zone A is about 1.0 at $t = 0.38$. This suggests that large velocity differences (or shears) exist between particles and their surrounding fluid. A very strong mixing associated with large velocity differences can also be seen in Fig. 6 (at $t = 1.05$) between the spike- and bubble-like structures near the interface. Figures 6, 7, 8 show that whenever a particle jet is formed, neighbouring gas jets are always accompanied on either side of the particle jet. This phenomenon suggests that the formation and then growth of particle jets is subsequently promoted by the shear originating from the velocity differences between particles and their surrounding fluid. In general, the mesoscale results suggest that the initial fluid motion at the interface between the driver and the driven sections are triggered by the shock due to the presence of the densely-packed particles, which result in the formation of micro gas jets within voids in the innermost layer of the powder bed. At the same time, the outward motion of the innermost layer of particles, initially driven by the high pressure driver gas, results in a sequential inelastic collisions to chain particles radially, while the shears due to particle/gas-jet interactions cause the motion and inelastic collision (or clustering) of particles laterally. The heterogeneous nature of a fluid in the powder bed (with a high particle-to-fluid density ratio) also makes particle velocities significantly lower than those of the surrounding incipient gas jets at the early stage of shock acceleration. The velocity and density differences between the high-speed gas jets and the low-speed moving particles result in large shears. This further promotes clustering and agglomeration of particles into a coherent particle-jet structure and transfers the energy from shock waves to the disseminated particles. Overall, we believe that the most probable underlying causes for the formation of particle jet structures are the driver gas jet flow induced by the shock wave as it passes through the initial gaps between the particles in the innermost layer of the powder bed, and the chaining of solid particles by inelastic collision. The subsequent shear flow between particles and surrounding fluid further accelerates the particle jet formation and growth.

As observed above, the particle jet structure emerges in a very early time. A clear definition of the particle jet forming time will help the researchers working on macroscopic (multiphase) simulations to determine the start and end times during which the "effective drag" models (see, e.g., [5]) can be applied. Two options of determining the particle jet forming time are suggested here based on the present mesoscale simulations. The first option is to use the time when the divergence of particle velocity is zero (viz., all particles in a particle jet move at the same speed) except at $t = 0$:

$$\nabla \cdot V_{\mathrm{p}} = 0. \tag{25}$$

A particle jet in Zone A illustrated in Fig. 6 is further analyzed below, and the particles in question are numbered as shown in Fig. 9. For each labeled particle within the particle jet, the time histories of the aerodynamic force exerted on each particle and particle velocity are obtained from our mesoscale simulations and illustrated in Figs. 10 and 11 for their x- and y-components, respectively. As shown in both figures, after initial perturbations in an early time when particle jets are formed, the x- and y-components of the aerodynamic force, $|F_x|$ and $|F_x|$, decrease towards zero, suggesting that all particles move at almost the same speed (i.e., $\nabla \cdot V_{\mathrm{p}} \to 0$) when $t \approx 0.4$, at which clusters of particles are formed through collision. Hence, the time when (25) is satisfied may be considered as the jet forming time.

While the jet structures inside the powder bed are forming, the outer surface of the powder bed is expanding ahead of the shock fronts between $t = 0.38$ and 0.74 as shown in Figs. 6 and 7. The corresponding time can also be chosen as the second option to determine the jet forming time. Since the movement of the outer surface of the powder bed can be detected in both experiments and numerical simulations, the

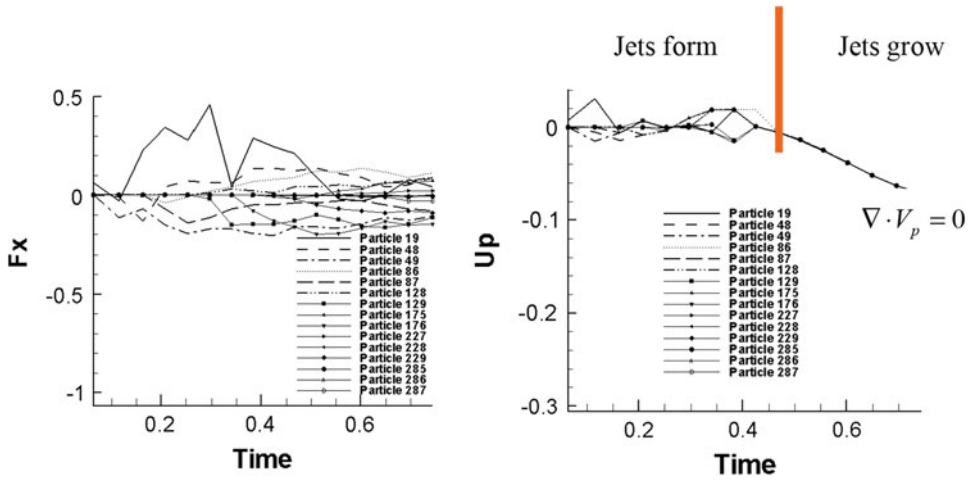

Fig. 10 The x-component of the dimensionless aerodynamic force and particle velocity. Dimensionless groups are defined in (24)

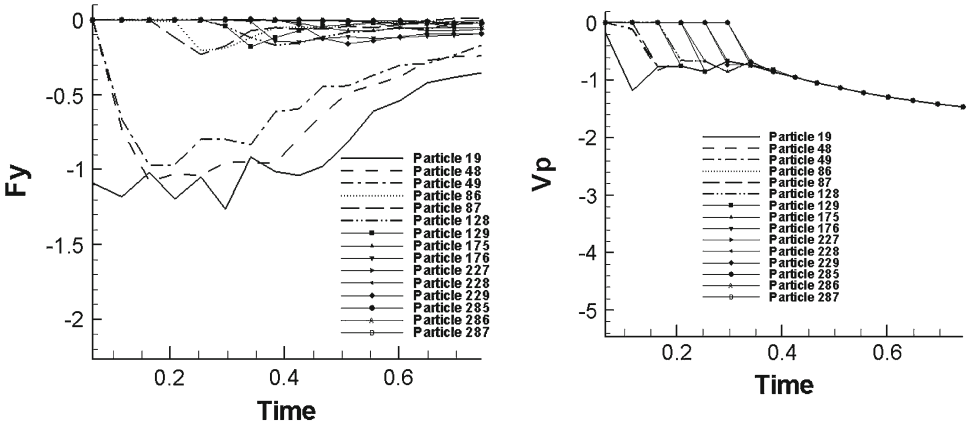

Fig. 11 The y-component of the dimensionless aerodynamic force and particle velocity. Dimensionless groups are defined in (24)

jet forming time defined in this way is likely more convenient than that determined by (25).

Physically, the motion of the outer surface of the powder bed is caused by the particle-to-particle collision and fluid movement within the voids between particles. The jet forming time based on the initial motion of the outer surface of the powder bed can therefore be estimated based on the average speed of the interstitial fluid within the voids of the powder bed, U, as:

$$t_{\text{jet}} = \frac{1}{2}\frac{D_{\text{p}} - D_{\text{c}}}{U} \tag{26}$$

where D_{p} is the diameter of the outer surface of the powder bed and D_{c} is the diameter of the central circular charge, which is the (high-pressure and high density) driver section in the present work.

The Gurney velocity, V_{G}, has been introduced in the past to describe the expansion velocity of a solid layer during fragmentation caused by detonation [18]. If $V_{\text{G}} \approx U$ is assumed, then:

$$V_{\text{G}} = \sqrt{2E_{\text{G}}}\left(\frac{M}{C} + \frac{1}{2}\right)^{-\frac{1}{2}} \tag{27}$$

where E_{G} is the Gurney constant mostly determined by the total energy of the charge (explosive or driver section) and M/C is the mass ratio of powder bed to charge. In this work, U in (26) is estimated using the shocked fluid velocity, and the corresponding jet forming time is determined to be at around $t = 0.6$ for the "Basic" test case, which is larger than that at around $t = 0.4$ obtained with (25) based on $\nabla \cdot V_{\text{p}} = 0$.

4 Parameters affecting the number of particle jets

In the experiments of a packed bed of solid particles dispersed through detonation of a cylindrical explosive, the number of the particle jets increases with the diameter (i.e., the mass) of the explosive and decreases with the thickness or the mass of the powder bed [5].

For a given mass and configuration of a powder bed, there is a threshold mass of explosive corresponding to a threshold particle expansion velocity, below which the outer surface of

the powder bed remains smooth and above which incipient instabilities develop to form particle clusters and coherent jet structures [3]. Frost et al. [3] introduced a compaction Reynolds number and found that the threshold corresponded to a critical compaction Reynolds number, above which the number of particle jets increased with the compaction Reynolds number. This Reynolds number was defined as the ratio of the inertial force of particles to the viscous force during the shock compaction of the powder bed,

$$Re_{\text{compact}} = \frac{\rho_{\text{p}} V_{\text{p}} L_{\text{p}}}{\mu_{\text{c}}} \tag{28}$$

where ρ_{p}, V_{p}, L_{p}, and μ_{c} are the concentration of particles, maximum expansion velocity of particles, layer thickness and the effective compaction viscosity of the particle layer. $\mu_{\text{c}} = \gamma_{\text{s}} c_{\text{s}} d_{\text{s}}$, in which γ_{s}, c_{s} and d_{s} are the material density, sound speed and diameter of a solid particle. While the compaction Reynolds number was found to be related to the total number of particle jets, a quantitative empirical correlation for the total number of particle jets is yet to be determined.

Ripley et al. [5] analyzed the data in [4] and fitted the experimental number of particle jets into a function of the Gurney velocity, which was the expansion velocity at the outer surface of the powder bed or into a function of the fluid pressure, P_{fluid}, at the outer surface of the powder bed based on their numerical simulations at macroscale:

$$N_j = 87 + V_{\text{G}}/9.3 + V_{\text{G}}^2/20{,}000 \tag{29}$$

or

$$N_j = 129 P_{\text{fluid}}^{0.13} \tag{30}$$

where V_{G} is in mm/μs and P_{fluid} is in GPa. Note that (29) and (30) have been fitted to the atomized aluminum particles above the threshold mass ratio of explosive to powder bed, and cannot be applied extensively to other types of particles, for which material density of particles, restitution coefficient and other morphology parameters are different.

To explore the dependence of the number of particle jets on various parameters, mesoscale simulations using the HLLC3D-IBM code have been carried out for a variety of cases listed in Table 5. The parameters varied include the total number of particles, particle size, particle material density, pressure ratio between the driver and the driven sections, random versus uniform particle distributions, restitution coefficient [recall (17)], and the number of particles in the innermost layer of the powder bed. For each test case, we change one parameter at a time in order to compare the results with the "Basic" test case discussed in the previous section. For instance, for the test case entitled "Pressure2" in row 6 of Table 5, the pressure ratio of 10:1 is employed instead of 100:1 as in the "Basic" test case. The test case entitled "Particle density" contains half of the particles with the dimensionless particle material density of 10, and the other half of the particles with the dimensionless particle material density of 50. If the "Randomness" test case is labeled as "no", it means that particles are uniformly distributed for all layers, and all particles distributed in the same (ring-shaped) layer are at the same radius from the center of the driver section. Since the size of the computational domain is fixed to be 9.6×9.6 in a dimensionless unit, the particle size listed in the "Particle size" test case in row 5 of Table 5 is 0.05 in radius for evenly numbered particles, and 0.03 in radius for oddly numbered particles. The restitution coefficient is introduced in the collision model described in (17). The zero restitution coefficient for the "Restitution" test case in Table 5 means that collision is fully inelastic, while collision is partially elastic and partially inelastic when the restitution coefficient is equal to 0.5 for two-particle collision scenarios. To reduce programming efforts, the restitution coefficient is assumed to be zero for multiple particle collision scenarios, involving more than two particles. The purpose of these tests was to find the relationship between each parameter (such as the total number of particles, pressure ratio, density ratio, particle size, restitution coefficient, etc.) and the number of particle jets.

As shown in Table 5, there are 7 ring-shaped layers for most test cases, and the number of particles for each layer is listed in Table 4 with 300 particles in total in the computational domain. The number of particles increases gradually as the radius of each layer increases. The test cases entitled "Layer3" and "Layer5" employ only the first three and five layers in Table 4, respectively. Therefore, the "Layer3" case has 96 particles and the "Layer5" case has 187 particles in total. While almost all the test cases in Table 5 have 25 particles in the innermost layer, the case entitled "Inner layer" in the last row of Table 5 is an exception. The "Inner layer" case involves 183 particles in total, with the particle size of 0.1 in radius. They are configured in 6 layers, in which 17 (instead of 25) particles are distributed in the innermost layer. For all cases listed in Table 5, the particle volume fraction is between 0.20 (for the "Particle size" case) and 0.56 (for the "Inner layer" case).

From the mesoscale simulations, the total number of particle jets for each test case is counted when they are fully developed and are listed in the third last column of Table 5. The patterns of the particle jets are maintained after the formation of jet structure is completed in early times—a phenomenon observed in the experiments as well [3–5]. As shown in the first four rows of Table 5, the number of particle jets decreases as the inertia of the powder bed increases (i.e., an increase in either the total particle number or the material density of particle) at a given driver pressure. The effect of particle size on the number of particle jets is not apparent within the size range studied (only two sizes are investigated here). Furthermore, as shown in the first, sixth and seventh rows of Table 5, namely, the "Basic", "Pressure2" and "Pressure3" cases, the number of particle jets increases as the driver pres-

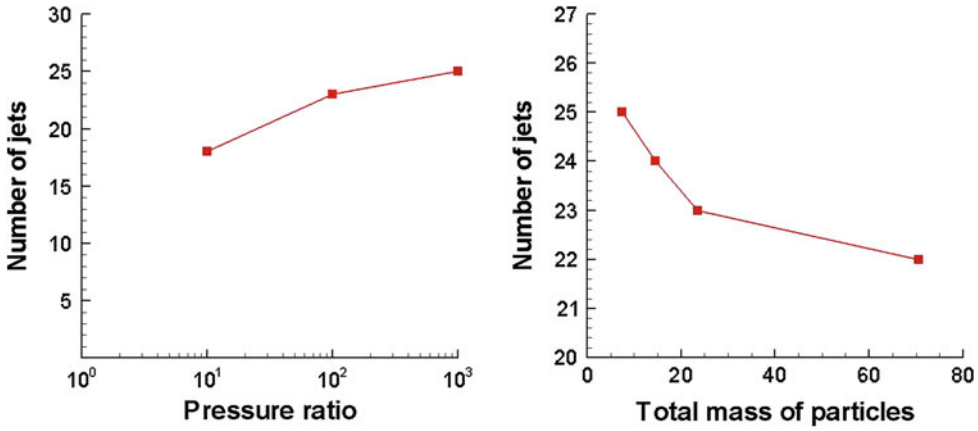

Fig. 12 The number of particle jets vs. the pressure ratio (*left*) and the dimensionless total mass of particles (*right*). Dimensionless groups are defined in (24)

sure increases. An increase in the driver pressure serves as the main driving force for particle dispersal. The trends in relation to how the total number of particle jets varies with a change in inertia (or mass of the powder bed), driver pressure and particle size are in good agreement with the experiments in [3–5], although the high explosive used for the dispersal of particles is simplified to a (high-pressure and high-density) driver section without chemical reactions in this paper. Figure 12 shows the number of particle jets as a function of pressure ratio of driver gas to ambient air (left subfigure), and as a function of total mass of particles in the powder bed (right subfigure). Both subfigures are in good agreement with the experimental fitting of (29) and (30) qualitatively, where the Gurney velocity V_G is a monotonically increasing function of the mass ratio of explosive to powder bed.

The number of particle jets also depends on how particles are packed in the powder bed, as indicated in the "Random" test case listed in row 8 of Table 5. In comparison with the "Basic" test case, the number of particle jets is reduced from 23 to 21, indicating that higher resistance exists for the randomly-packed case compared to the uniformly-packed case. The number of particle jets remains unchanged when the restitution coefficient is increased from 0 (fully inelastic) to 0.5 (partial inelastic). A value of the restitution coefficient chosen to be between 0 and 0.5 appears realistic in the high explosive dispersal of particles, where the shock pressure can reach several gigapascals in the early compaction phase of detonation, so that most of the particle collisions can be considered as inelastic collision. More simulations, which are numerically challenging due to very small time steps required to ensure numerical stability, may still be needed for the restitution coefficient to be above 0.5.

From all the cases investigated herein, it appears that the maximum number of particle jets is closely related to the number of particles in the innermost layer of the powder bed. This is consistent with the mechanisms for the formation of particle jet structures studied in the previous section, that is, the gas jet flow induced by the shock wave as it passes through the initial gaps between the particles in the innermost layer of the powder bed, and the chaining of solid particles by inelastic collision. The number of micro gas jets at the interface between the driver section and the powder bed must be the same as the number of particles in the innermost layer of the powder bed. As the number of particle layers increases or the driver pressure decreases, for instance, some perturbations at the interface caused by the passage of shocks may not develop into micro gas jets. Alternatively, the micro gas jets developed may not be strong enough and are damped out rapidly as they pass through layers of particles, resulting in a fewer number of particle jets than the number of particles in the innermost layer of the powder bed. Among all the first nine test cases (except the "Inner layer" case) in Table 5, the innermost layer has 25 particles. Case "Layer3" (with the least particle layers) and Case "Pressure3" (with the highest pressure ratio) generates 25 particle jets, while the rest of the cases produce fewer particle jets.

In order to further confirm that the maximum number of particle jets must be consistent with the number of particles in the innermost layer of the powder bed, a new test case entitled "Inner layer" shown in the last row of Table 5 is created with a powder bed configuration different from those listed in Table 4. Figure 13 shows its mesoscale simulation result at a late time (i.e., the particle jets are fully developed) compared with the result of the "Layer3" case that has 25 (instead of 17) particles in the innermost layer of the powder bed. The number of fully developed particle jets is 17 for the "Inner layer" case and 25 for the "Layer3" case. This further confirms that the maximum number of particle jets is solely determined by the number of particles in the innermost layer of the powder bed.

Following the above parametric studies to investigate the mechanisms for the formation of particle jets, an empirical formula to estimate the number of particle jets is proposed:

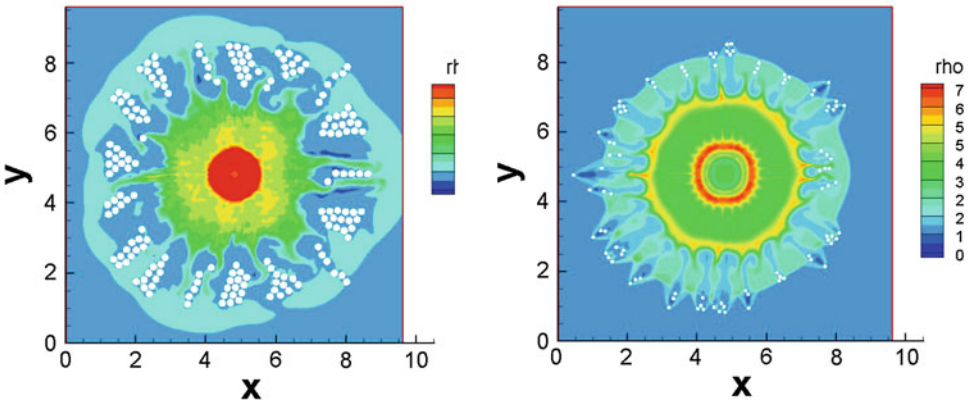

Fig. 13 Dimensionless density contours at $t = 3.3$ for the "Inner layer" case with 17 particles in the innermost layer (*left*), and at $t = 1.4$ for the "Layer3" case with 25 particles in the innermost layer (*right*). Dimensionless groups are defined in (24)

$$N_{\text{jet}} = \text{int}\left(\alpha \frac{\pi D_{\text{c}}}{d_{\text{s}} + \beta}\right) \tag{31}$$

where D_{c}, d_{s} and β are the diameter of the driver section, mean particle diameter and the average gap between particles (0.025 in this work), respectively. The term $\frac{\pi D_{\text{c}}}{d_{\text{s}}+\beta}$ represents the maximum number of particles placed in the innermost layers of a cylindrical powder bed to give a maximum or upper bound of the total number of particle jets. This term can be easily extended for a spherical configuration. In (31), α is a function that depends on all other main parameters (see Table 5) affecting the number of particle jets. Assuming inelastic collision and without considering the influence of random particle distributions for simplicity, α can be assumed to be dependent upon the mass ratio of powder bed to charge (or the driver section in this work), M/C. This includes the total number of particles, the material density of the particle and the mass of the charge (or the pressure ratio of driver gas to air in this work). Note that the mass of the powder bed shall also include the mass of interstitial fluid. In the following, the mass of interstitial air is negligibly small compared to the mass of solid particles. Therefore, M/C represents the inertia force of the powder bed to the driving force in the driver section. M/C determines directly the particle expansion velocity of the outer surface of the powder bed [i.e., the Gurney velocity defined in (27)]. Hence, α is postulated to be correlated with M/C as:

$$\alpha = 1 - m\left(\frac{M}{C} + b\right)^n \tag{32}$$

where m, n and b are the model constants. In this work, the density ratio of driver gas to air is the same as the pressure ratio. The charge mass in (32) is therefore replaced by pressure ratio:

$$\alpha = 1 - m\left(\frac{M^*}{P^*} + b\right)^n \tag{33}$$

where M^* and P^* are the dimensionless mass of total particles and pressure ratio of driver gas to air, respectively. Equation (31) used to estimate the total number of particle jets is then rewritten in the following form:

$$N_{\text{jet}} = \text{int}\left[\left(1 - 0.075\left(\frac{M^*}{P^*} + 0.7\right)^{1.02}\right)\frac{\pi D_{\text{c}}}{d_{\text{s}} + \beta}\right] \tag{34}$$

where the coefficients are obtained by curve fitting based on our mesoscale results. The estimated numbers of particle jets based on (34) are listed in the second last column of Table 5. For most cases listed in Table 5, a very good agreement between the number of particle jets counted from our mesoscale solutions and that estimated by (34) is achieved, and the maximum discrepancy is by two jets (i.e., the "Inner layer" case). More mesoscale simulations under different configurations of powder bed and driver (e.g., different driver sizes) are needed to further verify this formula.

5 Concluding remarks

The present work is stimulated by the interest in understanding the physical mechanisms associated with explosive dispersal of dense solid particles, where the particle clustering and coherent jet formation are observed in a number of experiments. Clustering and coherent jetting of particles are fundamental phenomena in supersonic dense particle flows. To gain a better understanding of jetting of particles, a cylindrical shock tube problem, in which a central high pressure/high density driver section surrounded by a densely packed powder bed in air in the driven section, is investigated. Mesoscale simulations are conducted to study this cylindrical shock tube problem of dense solid particle flows by solving the two-dimensional Navier–Stokes equation. The GCIBM and a novel multi-particle inelastic collision model are incorporated in our HLLC3D-IBM code to perform numerous simulations. Parameters varied include the driver gas pressure, particle distribution, particle morphology and packed powder bed configuration; the last three include the number of particle layers, number of particles in each layer, material density of particle, particle size, uniform versus random particle distributions and restitution coefficient.

The simulation results indicate that as the shock passes through the interface between the driver section and powder bed, micro gas jets are formed in voids between particles in the innermost layer of the powder bed. The gas jets penetrate the powder bed in a radial direction and propel the particles laterally. These micro gas jets also incur a large shear due to velocity differences between particles and their surrounding fluid, a phenomenon which further propels particles laterally to form clusters of particles. At the same time, the high pressure driver gas pushes the particles in the innermost layer of the powder bed to collide with particles in the subsequent layers to form chains of solid particles by inelastic collision. As a result, particles in the outermost layer of the powder bed start to move while shocks are still immersed in the powder bed. The number of micro gas jets at the interface between the driver section and the powder bed must be the same as the number of particles in the innermost layer of the powder bed. In summary, we believe that the formation of micro gas jets close to the interface induced by the shock wave as it passes through the initial gaps between the particles in the innermost layer of the powder bed, and the inelastic particle collision are the dominant mechanisms for the clustering of particles and formation of particle jets. The time for the jet formation process is very short and the jet forming time is estimated by the time when the motion of the particles at the outermost layer of the powder bed is distinguishable.

Since the number of micro gas jets must be the same as the number of particles in the innermost layer of the powder bed, the latter provides a maximum or upper limit of the number of particle jets as demonstrated in our mesoscale simulations. As the mass of the powder bed (related to the total number of particles, number of particle layers and material density of particle) increases or the driver pressure decreases, some weak perturbations at the interface between the driver section and the powder bed, caused by the passage of the shocks, may not develop into sustainable micro gas jets to fracture the powder bed. This results in fewer particle jets than particles in the innermost layer of the powder bed. Thus, the number of particle jets after the jet forming time is mainly a function of the number of particles in the innermost layer of the powder bed adjacent to the driver section, and the mass ratio of powder bed to charge or the ratio of the dimensionless powder bed mass to the pressure ratio of driver to air. The random distribution of particles could further reduce the number of particle jets formed due to high local resistance. Scenarios involving elastic collision will require further investigation in the future.

The diverging shock tube problem (either cylindrical or spherical), involving dense solid particles, is very fundamental. The real-world-scale dispersal of a densely-packed solid particle bed through detonation of a central explosive is much more complicated and will involve additional physical mechanisms not accounted for in the present model. The numerical solutions of a two-dimensional cylindrical shock tube problem, involving densely-packed solid particles, and the underlying mechanisms studied herein may only provide insights into some fundamental aspects of the very sophisticated real-world-scale problems. For instance, the real world problems may contain millions or trillions of solid particles, in which the agglomerated super-particles at the explosive interface might be considered as "particles" in the innermost layer of the powder bed. In the real world problems, the explosive is often contained in a thin casing made of metal, glass or cardboard. The fragments of the casing could also be regarded as "particles" of the innermost layer. Furthermore, in the real world problems, solid particles may need to be held in a container. The fragmentation of the container would introduce additional mechanisms, which further influence the particle jet structure and number. Nevertheless, the driving power (detonation of explosive and subsequent shock wave), particle morphology, particle distribution and the particle bed configuration are always the main factors for the clustering and formation of coherent jet structure in the resulting dense solid particle flow. The diverging shock tube flow containing solid particles provides a good starting point to study the fundamental aspects of a supersonic dense solid particle flow, which remains an open area. Extension of the present work to re-examine factors such as more particles in the powder bed, higher pressure and density ratios corresponding to high explosive, particle deformation, compaction effects that occur at these pressures, particle casing effects, combustion and finer meshes will require further investigations.

Finally, it should be emphasized here that the subject matter of the present study is about a dense solid particle flow with a particle volume fraction of 0.1–0.6, where the direct particle interactions and the intensive interactions between the particles and void fluid are unique and critically important. Recent studies related to multiphase RM instability (e.g., [17]) and clustering of particles (e.g., [19]) at macroscale adapted a continuum approach of essentially dilute multiphase flow without the above-mentioned interactions, and are different from the phenomena reported in the present study. Other recent papers [20,21] discussing the clustering of particles during explosive particle dispersal are cited here for the purpose of completeness for interested readers.

Acknowledgments This work was made possible by the facilities of the Shared Hierarchical Academic Research Computing Network (SHARCNET: http://www.sharcnet.ca) and Compute/Calcul Canada.

References

1. Milne, A.M., Parrish, C., Worland, I.: Dynamic fragmentation of blast nitigants. Shock Waves **20**, 41–51 (2010)
2. Ritzel, D.F., Ripley, R.C., Murray, S.B., Anderson, J.: Near-field blast phenomenology of thermobaric explosions. In: Hannemann,

K., Seiler, F. (eds.) Proceedings of the 26th International Symposium on Shock Waves, 15–20 July 2007, pp. 281–286. Springer, Gottingen, Germany (2007)
3. Frost, D.L., Grégoire, Y., Goroshin, S., Zhang F.: Particle jet formation during explosive dispersal. In: Proceedings of the 23rd International Colloquium on the Dynamics of Explosions and Reactive Systems (ICDERS), 24–29 July 2011, Irvine, California, USA (2011)
4. Zhang, F., Yoshinaka, A., Ripley, R.C.: Hybrid detonation waves in metalized explosive mixtures. In: Proceedings of the 14th International Detonation Symposium, 11–16 April 2010, pp. 714–723. Coeur d'Alene, Idaho, USA (2010)
5. Ripley, R.C., Donahu, L., Zhang, F.: Jetting instabilities of particles from explosive disposal. In: Proceedings of the Shock Compression of Condensed Matter-2011, American Institute of Physics, 26 June-1, July 2011, pp. 1615–1618. Chicago, IL, USA (2011)
6. Boris, J., Grinstein, F., Oran, E., Kolbe, R.: New insights into large eddy simulation. Fluid Dyn. Res. **10**, 199–228 (1992)
7. Tseng, Y.H., Ferziger, J.H.: A ghost-cell immersed boundary method for flow in complex geometry. J. Comput. Phys. **192**, 593–626 (2003)
8. Lien, F.S., Xu, T., Zhang, F.: The role of vorticity and turbulence on the instability of a dense solid particle flow. In: Proceedings of the Shock Compression of Condensed Matter-2011, American Institute of Physics, 26 June-1 July 2011, pp. 1619–1622. Chicago, IL, USA (2011)
9. Toro, E.F.: Riemann Solvers and Numerical Methods for Fluid Dynamics. Springer, Berlin (1997)
10. Xu, T., Ji, H., Lien, F. S., Zhang, F.: Numerical simulations with an immersed boundary method pertinent to multiphase turbulent flows. In: Proceedings of the 17th Annual Conference of the CFD Society of Canada, 3–5 May 2009. Ottawa, ON, Canada (2009)
11. Sagaut, P.: Large Eddy Simulation for Incompressible Flows: An Introduction. Springer, Berlin (2005)
12. Ripley, R., Lien, F.S., Yovanovich, M.M.: Numerical simulation of shock diffraction on unstructured meshes. Comput. Fluids **35**, 1420–1431 (2006)
13. Brilliantov, N.V., Poschel, T.: Kinetic Theory of Granular Gases. Oxford University Press, Oxford (2004)
14. Bouris, D., Bergeles, G.: 2D LES of vortex shedding from a square cylinder. J. Wind Eng. Ind. Aerodyn. **89**, 31–46 (1999)
15. Schilling, O., Jacobs, J.W.: Richtmyer-Meshkov instability and re-accelerated inhomogeneous flows. Scholarpedia **3**, 6090 (2008). doi:10.4249/scholarpedia.6090
16. Keselev, V., Keselev, S., Vorothzsov, E.: Interaction of a shock wave with a particle cloud of finite size. Shock Waves **16**, 53–64 (2006)
17. Ukai, S., Balakrishnan, K., Menon, S.: On Richtmyer-Meshkov instability in dilute gas-particle mixtures. Phys. Fluids **22**, 104103 (2010)
18. Gurney, R. W.: The initial velocities of fragments from bombs, shells, and grenades. BRL Report 405, Ballistic Research Laboratory, Aberdeen, Maryland, USA (2003)
19. Balakrishnan, K., Ukai, S., Menon, S.: Clustering and combustion of dilute aluminum particle clouds in a post-detonation flow field. Proc. Combust. Inst. **33**, 2255–2263 (2011)
20. Frost, D.L., Grégoire, Y., Petel, O., Goroshin, S., Zhang, F.: Particle jet formation during explosive dispersal of solid particles. Phys. Fluids **24**, 091109 (2012)
21. Grégoire, Y., Sturtzer, M.O., Khasainov, B., Veyssiere, B.: Investigation on the dispersion of solid particles by high explosive. In: Proceedings of the 27th International Symposium on Shock Waves, 19–24 July 2009, St. Petersburg, Russia, pp. 156–162 (2009)